

## Numerical Simulation of 2-D Wing-In-Ground Effect

Chen-Jun Yang\*<sup>1</sup> and Myung-Soo Shin\*<sup>2</sup>

### 2 차원 해면효과의 수치계산

Chen-Jun Yang\*<sup>1</sup>, 신명수\*<sup>2</sup>

본 논문은 2 차원 해면효과의 수치계산 결과를 정리하였다. 지면으로부터의 높이변화에 따른 점성유동장을 계산하기 위하여 지배방정식으로는 비압축성 RANS 방정식을, 시간에 대하여서는 음해법으로 프로그램을 구성하였다. 압력항은 가상압축성과 4 차 수치확산항을 추가하는 것에 의해 계산하였으며, 높은 레이놀즈수에서의 효과적인 계산을 위해 Baldwin-Lomax 난류모델을 도입하였다. 해면효과가 없는 무한유종에서의 NACA-0012 단면 계산결과를 실험 데이터와 비교하는 것에 의해 프로그램의 타당성을 확인하였다. NACA-6409 와 두께 비 4.6%의 날개에 대하여 해면효과를 고려한 계산을 수행하였다. 계산결과, 높이의 변화에 따라 계산된 무차원계수, 압력 및 속도분포는 해면효과의 특성을 잘 보여주고 있다.

**Keywords :** 해면효과(Wing-In-Ground Effect), RANS 방정식(Reynolds Averaged Navier-Stokes Equation), 음해법(Implicit Method), 가상압축성(Pseudo compressibility), Baldwin-Lomax 난류모델(Baldwin-Lomax Turbulence Model)

### 1. Introduction

It is well-known that the lift force of a wing is increased when it approaches the ground or water surface, but the practical research and development of Wing-In-Ground effect vehicles (WIGs) which take the advantage of this knowledge were not made until 1960's. Many pioneering works on the wing were

done in the former USSR for military purposes. In recent years, as a result of the increasing demand for high-speed sea transportation, the interest in the WIG vehicles is rising in many countries because they are especially competent for midium-range passenger and cargo transport.

In such a situation researches on the WIG are stimulated correspondingly. In fact, there remain some critical problems such as the stability, which requires careful attention in designing WIGs. For this purpose,

\*<sup>1</sup> Shanghai Jiao Tong University, China; presently visiting professor at KRISO

\*<sup>2</sup> Member, Korea Research Institute of Ships and Ocean Engineering (KRISO)

detailed flow phenomena and aerodynamic performances of WIGs need to be investigated. It is then natural that CFD provides a useful tool for them along with experimental research.

Recently Hirata[1,2] and Hirata et al.[3] presented their researches on the WIG by using a finite-volume method. In the research of Kim et al.[4], the problem of longitudinal stability was investigated numerically for 2-D(two-dimensional) WIG with a finite-difference method.

In the present research, we use RANS Equation. That is a part of our research aimed at viscous flow simulation for WIGs.

The pseudo-compressibility formulation proposed by Chorin[5] is adopted in the present method. The approximate factorization technique is used to solve the Reynolds Averaged Navier-Stokes (RANS) equations. The convective terms in momentum equations are approximated with third-order upwind differencings. Fourth-order central differencings are used for the other spatial derivatives, and fourth-order numerical dissipation terms for pressure are added implicitly into the continuity equation to damp out the high-frequency pressure oscillations[6].

The Baldwin-Lomax turbulence model[7] is used to simulate high-Reynolds-number flows.

NACA0012 section was calculated first by using the present method. The results are compared with experimental data, and the accuracy of the present numerical scheme for 2-D unbounded flow is verified.

Numerical investigations into the ground effect are made for two NACA four-digit sections, NACA6409 and another one of 4.6% thickness and 0.358% camber ratio. The present scheme is found to be quite stable, and its convergence rate is very fast especially under strong ground effect.

## 2. Numerical Formulation

### 2.1 Governing equations

The 2-D RANS equations with pseudo-compressibility are written in vector form as follows:

$$q_t + Fq_x + Gq_y = C_R(q_{xx} + q_{yy}) \quad (1)$$

where

$$q = \begin{bmatrix} u \\ v \\ p \end{bmatrix}, \begin{cases} F = F_c + F_v \\ G = G_c + G_v \end{cases}$$

$$F_c = \begin{bmatrix} u & 0 & 1 \\ 0 & u & 0 \\ \beta & 0 & 0 \end{bmatrix}, G_c = \begin{bmatrix} v & 0 & 0 \\ 0 & v & 1 \\ 0 & \beta & 0 \end{bmatrix},$$

$$F_v = \begin{bmatrix} -2v_x & -v_y & 0 \\ 0 & -v_x & 0 \\ 0 & 0 & 0 \end{bmatrix}, G_v = \begin{bmatrix} -v_y & 0 & 0 \\ -v_x & -2v_y & 0 \\ 0 & 0 & 0 \end{bmatrix}$$

$$C_R = \left(\frac{1}{R_e} + \nu_t\right) \begin{bmatrix} 1 & 0 & 0 \\ 0 & 1 & 0 \\ 0 & 0 & 0 \end{bmatrix}$$

$u$  and  $v$  denote velocity components in  $x$  and  $y$  directions, respectively. The subscripts  $x$ ,  $y$  and  $t$  denote partial derivatives.  $p$  is the pressure,  $R_e$  is the Reynolds number defined as  $R_e = U_0 L / \nu$ . All the variables are nondimensionalized by the characteristic length of body,  $L$ , and the inflow velocity,  $U_0$ , except the pressure,  $p$ , which is nondimensionalized by  $\rho U_0^2$ , where  $\rho$  is the density of fluid.  $\nu$  and  $\nu_t$  are kinematics viscosity and local eddy viscosity respectively.  $\beta$  is a positive constant for pseudo-compressibility.

### 2.2 Solution in boundary-fitted coordinates

Numerical solution of the governing equations is carried out in boundary-fitted coordinates to facilitate the implementation of body boundary conditions. The governing equations in physical coordinates  $(x,y)$  are transformed in terms of the boundary-fitted coordinates  $(\xi,\eta)$ , in which the computational domain is a rectangular area and the grids are of unit spacing in both coordinate directions.

The transformed governing equations read as follows:

$$q_t + Aq_\xi + Bq_\eta = C_R \nabla^2 q \quad (2)$$

where

$$\begin{cases} A = aF + dG \\ B = bF + eG \end{cases} \quad (3)$$

$$\nabla^2 q = \hat{\alpha}q_{\xi\xi} + \hat{b}q_{\eta\eta} + \hat{c}q_{\xi\eta} + \hat{g}q_\xi + \hat{h}q_\eta \quad (4)$$

$$J = 1/S = \frac{1}{x_\xi y_\eta - y_\xi x_\eta} \quad (5)$$

$$\left. \begin{aligned} a &= y_\eta / S \\ b &= -y_\xi / S \\ d &= -x_\eta / S \\ e &= x_\xi / S \end{aligned} \right\} \quad (6)$$

$$\left. \begin{aligned} S_\xi &= (ax_{\xi\xi} + bx_{\xi\eta} + dy_{\xi\xi} + ey_{\xi\eta})S \\ S_\eta &= (ax_{\xi\eta} + bx_{\eta\eta} + dy_{\xi\eta} + ey_{\eta\eta})S \end{aligned} \right\} \quad (7)$$

$$\left. \begin{aligned} \hat{a} &= a^2 + d^2 \\ \hat{b} &= b^2 + e^2 \\ \hat{d} &= 2(ab + de) \\ \hat{g} &= aa_\xi + ba_\eta + dd_\xi + ed_\eta \\ \hat{h} &= ab_\xi + bb_\eta + de_\xi + ee_\eta \end{aligned} \right\} \quad (8)$$

$$\left. \begin{aligned} a_\xi &= (y_{\xi\eta} - aS_\xi) / S \\ a_\eta &= (y_{\eta\eta} - aS_\eta) / S \\ b_\xi &= -(y_{\xi\xi} - bS_\xi) / S \\ b_\eta &= -(y_{\xi\eta} - bS_\eta) / S \\ d_\xi &= -(x_{\xi\eta} - dS_\xi) / S \\ d_\eta &= -(x_{\eta\eta} - dS_\eta) / S \\ e_\xi &= (x_{\xi\xi} - eS_\xi) / S \\ e_\eta &= (x_{\xi\eta} - eS_\eta) / S \end{aligned} \right\} \quad (9)$$

Equation (2) is discretized in time by using the Euler implicit scheme:

$$\frac{\Delta q^n}{\Delta t} + (Aq_\xi)^{n+1} + (Bq_\eta)^{n+1} = C_R^n \nabla^2 q^{n+1} \quad (10)$$

where superscript  $n$  denotes the  $n$ -th time step and

$$\Delta q^n = q^{n+1} - q^n \quad (11)$$

As the convective terms in (10) are nonlinear, they need to be linearized. The linearization is performed only for the inviscid part, while the viscous part is evaluated explicitly. Define

$$\left. \begin{aligned} U &= au + dv \\ V &= bu + ev \end{aligned} \right\} \quad (12)$$

$$A_c = \begin{bmatrix} U & 0 & a \\ 0 & U & d \\ a\beta & d\beta & 0 \end{bmatrix}, B_c = \begin{bmatrix} V & 0 & b \\ 0 & V & e \\ b\beta & e\beta & 0 \end{bmatrix} \quad (13)$$

Note that only the diagonal components in (13) are time-dependent and need to be linearized. Neglecting the second-order terms of  $\Delta q$  and/or its derivatives, we have

$$\begin{aligned} &(Aq_\xi)^{n+1} + (Bq_\eta)^{n+1} \\ &= (Aq_\xi)^n + (Bq_\eta)^n + (A\Delta q_\xi)^n + (B\Delta q_\eta)^n \\ &\quad + (\hat{A}\Delta q)^n + (\hat{B}\Delta q)^n \end{aligned} \quad (14)$$

where

$$\hat{A} = \begin{bmatrix} au_\xi & du_\xi & 0 \\ av_\xi & dv_\xi & 0 \\ 0 & 0 & 0 \end{bmatrix}, \hat{B} = \begin{bmatrix} bu_\eta & eu_\eta & 0 \\ bv_\eta & ev_\eta & 0 \\ 0 & 0 & 0 \end{bmatrix}.$$

Inserting the linearized convective terms into equation (10) and decomposing its right hand side, we have

$$\begin{aligned} &\{I + \Delta t[\hat{A} + A \frac{\partial}{\partial \xi} - C_R(\hat{g} \frac{\partial}{\partial \xi} + \hat{a} \frac{\partial^2}{\partial \xi^2}) \\ &\quad + I_p \omega^\xi \frac{\partial^4}{\partial \xi^4}]^n + \Delta t[\hat{B} + B \frac{\partial}{\partial \eta} - C_R \\ &\quad (\hat{h} \frac{\partial}{\partial \eta} + \hat{b} \frac{\partial^2}{\partial \eta^2}) + I_p \omega^\eta \frac{\partial^4}{\partial \eta^4}]^n\} \Delta q^n \\ &= \Delta t(C_R \nabla^2 q)^n - \Delta t(Aq_\xi + Bq_\eta)^n \\ &\quad + \Delta t C_R \hat{a} \Delta q_{\xi\xi}^{n-1} \\ &\quad + I_p (\omega^\xi \frac{\partial^4}{\partial \xi^4} + \omega^\eta \frac{\partial^4}{\partial \eta^4}) q^n \end{aligned} \quad (15)$$

where fourth-order numerical dissipation terms for pressure are added implicitly.  $\omega^\xi$  and  $\omega^\eta$  are positive constants.  $I_p$  is a matrix

$$I_p = \begin{bmatrix} 0 & 0 & 0 \\ 0 & 0 & 0 \\ 0 & 0 & 1 \end{bmatrix}.$$

Equation (15) is solved by the approximate factorization method. The solution procedure consists of two sweeps:

$\xi$ -sweep:

$$\begin{aligned} &\{I + \Delta t[\hat{A} + A \frac{\partial}{\partial \xi} - C_R(\hat{g} \frac{\partial}{\partial \xi} + \hat{a} \frac{\partial^2}{\partial \xi^2}) \\ &\quad + I_p \omega^\xi \frac{\partial^4}{\partial \xi^4}]^n\} \Delta q^\xi \\ &= \text{RHS of eq.(15)} \end{aligned} \quad (16)$$

$\eta$ -sweep:

$$\left\{ I + \Delta t \left[ \hat{B} + B \frac{\partial}{\partial \eta} - C_R \left( \hat{h} \frac{\partial}{\partial \eta} + \hat{b} \frac{\partial^2}{\partial \eta^2} \right) + I_p \omega^\eta \frac{\partial^4}{\partial \eta^4} \right] \right\} \Delta q^\eta = \Delta q^* \quad (17)$$

The present method employs third-order upwind differencings to discretize the convective terms for velocity, and fourth-order central differencings with numerical dissipation for pressure. This produces a set of block pentadiagonal equations for each sweep:

$\xi$ -sweep:

$$K_i \Delta q_{i-2}^* + L_i \Delta q_{i-1}^* + M_i \Delta q_i^* + N_i \Delta q_{i+1}^* + O_i \Delta q_{i+2}^* = \text{RHS of eq.(15)} \quad (18)$$

$\eta$ -sweep:

$$K_j \Delta q_{j-2}'' + L_j \Delta q_{j-1}'' + M_j \Delta q_j'' + N_j \Delta q_{j+1}'' + O_j \Delta q_{j+2}'' = \Delta q_j^* \quad (19)$$

where,

$$\left\{ \begin{aligned} K_i &= \bar{A} + \bar{C} + \frac{\Delta t}{12} (A_c + |A_c|) \\ L_i &= -8\bar{A} - \bar{B} + \frac{\Delta t}{3} (-2A_c - |A_c|) \\ M_i &= I + \Delta t \left( \hat{A} + \frac{5}{2} \hat{a} C_R \right) + 6\Delta t \omega^\xi I_p + \frac{\Delta t}{2} |B_c| \\ N_i &= 8\bar{A} - \bar{B} + \frac{\Delta t}{3} (2A_c - |A_c|) \\ O_i &= -\bar{A} + \bar{C} + \frac{\Delta t}{12} (-A_c + |A_c|) \\ \bar{A} &= \frac{\Delta t}{12} (A_v - \hat{g} C_R) \\ \bar{B} &= \Delta t \left( \frac{4}{3} \hat{a} C_R + 4\omega^\xi I_p \right) \\ \bar{C} &= \Delta t \left( \frac{1}{12} \hat{a} C_R + \omega^\xi I_p \right) \\ K_j &= \bar{A} + \bar{C} + \frac{\Delta t}{12} (B_c + |B_c|) \\ L_j &= -8\bar{A} - \bar{B} + \frac{\Delta t}{3} (-2B_c - |B_c|) \\ M_j &= I + \Delta t \left( \hat{B} + \frac{5}{2} \hat{b} C_R \right) + 6\Delta t \omega^\eta I_p + \frac{\Delta t}{2} |B_c| \\ N_j &= 8\bar{A} - \bar{B} + \frac{\Delta t}{3} (2B_c - |B_c|) \\ O_j &= -\bar{A} + \bar{C} + \frac{\Delta t}{12} (-B_c + |B_c|) \end{aligned} \right.$$

$$\left\{ \begin{aligned} \bar{A} &= \frac{\Delta t}{12} (B_v - \hat{h} C_R) \\ \bar{B} &= \Delta t \left( \frac{4}{3} \hat{b} C_R + 4\omega^\eta I_p \right) \\ \bar{C} &= \Delta t \left( \frac{1}{12} \hat{b} C_R + \omega^\eta I_p \right) \end{aligned} \right.$$

The subscripts  $i$  and  $j$  denote the numbering in  $\xi$ - and  $\eta$ -direction respectively. The coefficients,  $K_i \sim O_i, K_j' \sim O_j'$ , are 3x3 matrices.

Eqs. (18) and (19) are solved with a block pentadiagonal matrix solver. Then the velocity and pressure are updated and the computation proceeds to the next time step until a converged solution is reached.

The Baldwin-Lomax turbulence model[7] is used for turbulent flow simulation. The eddy viscosity is evaluated explicitly.

### 2.3 Initial and boundary conditions

The above finite difference equations are solved under appropriate initial and boundary conditions. For the present problem of Wing-In-Ground effect, H-type grids are used, and the computational domain is shown in Fig.1. The initial and boundary conditions are specified as follows:

- 1) *body surface*  
velocity:  $u=0, v=0$  (no-slip condition)  
pressure: zero-gradient along  $\eta$ -direction
- 2) *inflow (upstream) boundary*  
velocity:  $u=U_0, v=0$   
pressure:  $p=0$
- 3) *outflow (downstream) boundary*  
velocity: zero-gradient in  $\xi$ -direction  
pressure: zero-gradient in  $\xi$ -direction
- 4) *upper boundary*  
velocity: zero-gradient in  $\eta$ -direction  
pressure: zero-gradient in  $\eta$ -direction
- 5) *lower boundary (ground)*  
velocity:  $u=U_0, v=0$   
pressure: zero-gradient in  $\eta$ -direction
- 6) *initial condition (inside domain)*  
velocity:  $u=U_0, v=0$   
pressure:  $p=0$

lower surface, thus reduces the frictional resistance. Meanwhile, in the present case, a suction peak at the leading edge appears and gets larger as  $h/c$  decreases, as shown in Fig.9, which would cause the form drag to decrease. The center of pressure,  $X_{CP}$ , moves backwards as the wing approaches the ground

Fig.10 through Fig.13 are some examples of the calculated pressure and velocity field. It is observed that the increase in lift is mainly attributable to the higher pressure beneath the wing as a result of the blockage effect of the ground, since the pressure on suction side keeps almost unchanged.

### 3.3 NACA thin wing in ground effect

The thin wing section is of NACA 4-digit type, with 4.6% thickness ratio and 0.358% camber ratio (max. camber position at 0.2c). The computations were conducted at  $Re=10^6$  at  $3.5^\circ$  angle of attack.

Computation of the thin wing section is a little difficult as compared with the preceding case, mainly because of the sharp leading edge which produces a very high suction peak that makes the flow prone to separation.

The computation parameters are listed in Table 4. One can see that the maximum time step size is much smaller than that used for NACA6409, thus requiring much more steps to converge.

**Table 4** Computation parameters for thin wing

$H/c$	$NI \times NJ$	$\Delta t_{min}$	$\Delta t_{min}$	$\Delta t_{max}$
0.2	$128 \times 97$	0.0001	0.00025	0.001
0.1	$128 \times 97$	0.0001	0.00025	0.001
0.05	$128 \times 97$	0.0001	0.00025	0.001

The history of convergence for the thin wing is shown in Fig.14, which is quite similar to that shown in Fig.7 except for  $h/c=0.05$ , where high-frequency oscillations in  $C_L$  and  $C_D$  occur due to flow separation from the leading edge. It is to be verified by experiment whether the separation does occur or not. It should be noted that, if the oscillations do occur physically, time-accurate solutions would become necessary, and the present formulation employing the concept of pseudo-compressibility is only for steady solution.

Variations of lift, drag, and the pressure center are illustrated in Fig.15, and surface pressure distributions are shown in Fig.16.

Fig.17 and Fig.18 show calculated velocity and pressure field at  $h/c=0.1$ .

## 4. Concluding Remarks

A numerical method is presented in this paper for simulating the viscous flow around a 2-D Wing-In-Ground effect by solving the RANS equations. The concept of pseudo-compressibility is employed and an implicit finite difference method is used to solve the partial differential equations.

Numerical examples show that the present method is quite efficient and capable of simulating the flow phenomenon associated with Wing-In-Ground effect. An interesting feature of the present code is that it provides faster convergence at lower height ratio.

As our future work, the present method will be extended to 3-D, so that simulations can be made for more practical purposes.

## References

- [1] Hirata, H., "Simulation on Viscous Flow around Two-Dimensional Power-Augmented Ram Wing in Ground Effect," *Journal of the Society of Naval Architects of Japan*, Vol.174, pp.47-54, 1993.
- [2] Hirata, H., "Numerical Study on the Aerodynamic Characteristics of a Three-Dimensional Power-Augmented Ram Wing in Ground Effect," *Journal of the Society of Naval Architects of Japan*, Vol.179, pp.31-39, 1996.
- [3] Hirata, H. and Kodama, Y., "Flow Computation for Three-Dimensional Wing in Ground Effect Using Multi-Block Technique," *Journal of the Society of Naval Architects of Japan*, Vol.177, pp.49-57, 1995.
- [4] Kim, W.-J. and Shin, M.-S., "The Effects of Mean-Line Shape on Longitudinal Stability of a Wing in Ground Effect," *Journal of the Society of Naval Architects of Korea*, Vol.2, No.2, pp.14-23, 1996.
- [5] Chorin, A. J., "A Numerical Method for Solving Incompressible Viscous Flow Problems," *Journal Computational Physics*, Vol.2, pp.12-26, 1967.
- [6] Kodama, Y., "Computation of High Reynolds Number Flows Past a Ship Hull Using the IAF Scheme," *Journal of the Society of Naval Architects of Japan*, Vol.161, pp.24-33, 1987.
- [7] Baldwin, B. S. and Lomax, H., "Thin Layer Approximation and Algebraic Model for Separated Turbulent Flows," *AIAA Paper*, 78-257, 1978.
- [8] Abbott, I. H. and Doenhoff, A. E. von, "Theory of Wing Sections," *Dover Publications, Inc.*, 1959.

### 3. Numerical Examples

#### 3.1 NACA0012 in unbounded flow ( $h/c=\infty$ )

To test the performance of the computer code developed based on the present numerical method, computations were carried out for NACA0012 at  $Re=3 \times 10^6$  and  $6^\circ$  angle of attack, by using C- and H-grid respectively. The C-grid was generated by an elliptical equation method, while the H-grid by an algebraic method.

The computation parameters are listed in Table 1. NI and NJ are grid numbers in  $\xi$ - and  $\eta$ -direction respectively.  $\Delta_{min}$  is the minimum grid spacing,  $\Delta t_{min}$  and  $\Delta t_{max}$  are minimum and maximum time step size, respectively.

Fig.2 and Fig.3 show the C- and H-type grids used for NACA0012, respectively.

Table 1. Computation parameters for NACA0012

	NI×NJ	$\Delta_{min}$	$\Delta t_{min}$	$\Delta t_{max}$
C-grid	130×55	0.00005	0.001	0.01
H-grid	120×120	0.00005	0.00025	0.0025

Table 2. Comparison of  $C_L$  and  $C_D$

	$C_L$	$C_D$
Exp.[8]	0.64	0.0084
Cal. (C-grid)	0.636	0.0154
Cal. (H-grid)	0.682	0.0115

Fig.4 shows the convergence history of lift and drag coefficients,  $C_L$  and  $C_D$  (nondimensionalized by  $0.5\rho U_0^2$ ).

In Table 2, a comparison of calculated  $C_L$  and  $C_D$  with experimental data shows that the  $C_L$  given by C-grid agrees well with experiment, but that given by H-grid is overestimated. As for  $C_D$ , both grids yield higher values than experiment. It can be said that the present results show generally good agreement with experimental data.

In Fig.5 are shown the experimental and calculated surface pressure distributions, where the pressure coefficient,  $C_p$ , is nondimensionalized by  $0.5\rho U_0^2$ . The experimental points were reproduced from [1]. It is clear that, by using H-grid, the pressure difference between back and face sides are larger near the leading edge, which results in a larger lift. A possible reason

for the overestimation is, when using H-grid, the aspect ratio of grids near the leading edge have to be kept quite small in order to avoid pressure oscillation there. This makes the grids too much clustered towards  $\xi=const.$  line at the leading edge. Besides, in the case of H-grid kinks along  $\eta=const.$  lines are inevitable in the vicinity of the leading edge, which will also affect the accuracy.

Computations were also conducted for NACA6409 and another NACA 4-digit section of 4.6% thickness. It was found that, similar to the case of NACA0012, the calculated lift was slightly higher with H-grid than with C-grid.

#### 3.2 NACA6409 in ground effect

In this section, numerical results are presented for NACA6409 in ground effect at  $Re=2.37 \times 10^5$ , and  $4^\circ$  angle of attack. The computation parameters are listed in Table 3. The definition of height ratio,  $h/c$ , is shown in Fig.1, where  $c$  is section chord length. The H-grid at  $h/c=0.2$  is shown in Fig.6 as an example.

Fig.7 shows the convergence history of  $C_L$  and  $C_D$ . As the computation begins from a state of impulsive start, the initial time step size,  $\Delta t_{min}$ , has to be quite small. After about 2000 steps, the time step size can usually be increased by one order. Typically 4000 steps are needed to obtain a converged solution. For all the height ratios calculated, the same minimum and maximum time step sizes can be used and it converges faster as  $h/c$  decreases.

Table 3. Computation parameters for NACA6409

$h/c$	NI×NJ	$\Delta_{min}$	$\Delta t_{min}$	$\Delta t_{max}$
0.8	111×110	0.0001	0.0005	0.005
0.4	111×104	0.0001	0.0005	0.005
0.2	111×94	0.0001	0.0005	0.005
0.1	111×94	0.0001	0.0005	0.005
0.05	111×94	0.0001	0.0005	0.005
0.025	111×94	0.0001	0.0005	0.005
0.01	111×88	0.0001	0.0005	0.005

In Fig.8 are shown the computed variations of  $C_L$ ,  $C_D$ , and  $X_{CP}$  (the position of pressure center from the leading edge, in fractions of chord). The increase in lift is clearly observed with decreasing  $h/c$ . As for  $C_D$ , a slight decrease is found with decreasing  $h/c$ . This seems rational because the blockage effect of the ground makes smaller velocity gradient beneath the

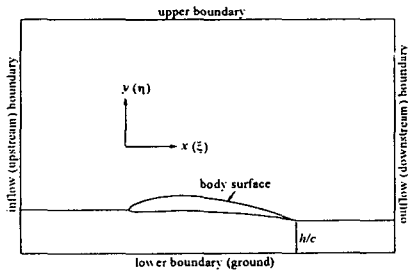


Fig. 1 Domain of computation

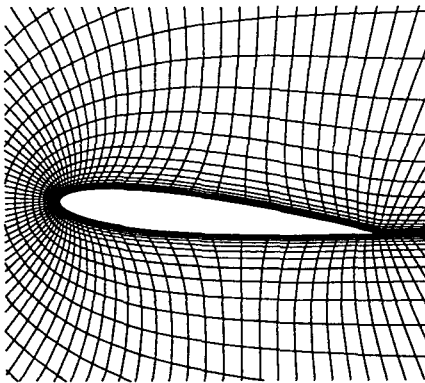


Fig. 2 C-grids for NACA0012

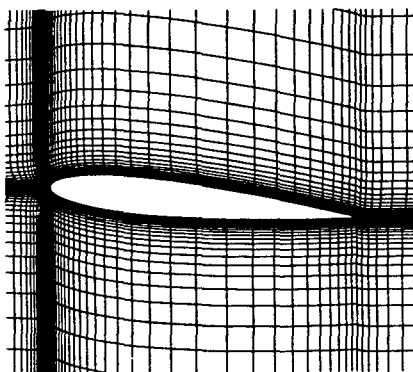


Fig. 3 H-grids for NACA0012

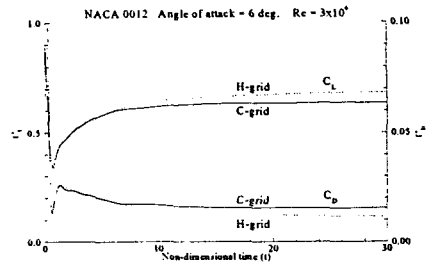


Fig. 4 Convergence history for NACA0012

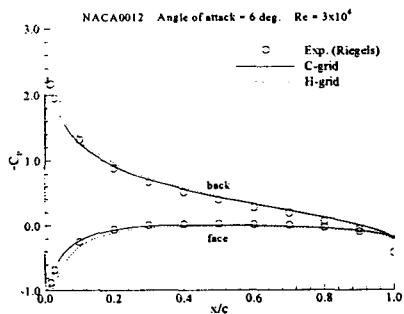


Fig. 5 Comparison of surface pressure

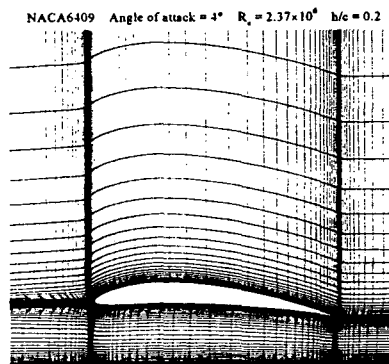


Fig. 6 H-grid for NACA6409 at h/c=0.2

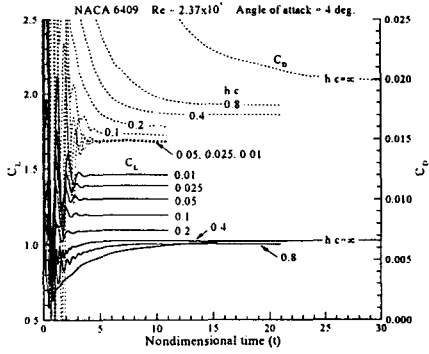


Fig. 7 Convergence history of NACA6409

NACA 6409  $Re = 2.37 \times 10^5$  Angle of attack = 4 deg.  $h/c = 0.1$

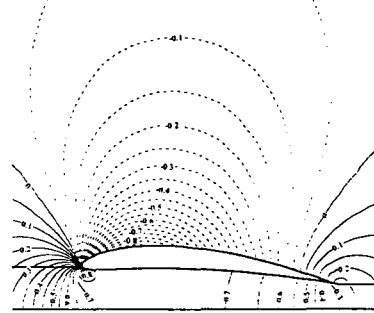


Fig. 10 pressure field around NACA6409,  $h/c=0.1$

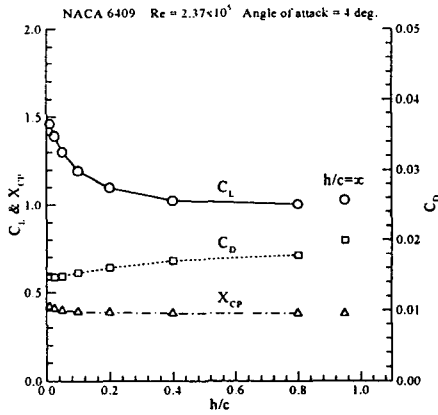


Fig. 8 Variation of  $C_L$ ,  $C_D$ ,  $X_{CP}$  with  $h/c$

NACA 6409  $Re = 2.37 \times 10^5$  Angle of attack = 4 deg.  $h/c = 0.1$

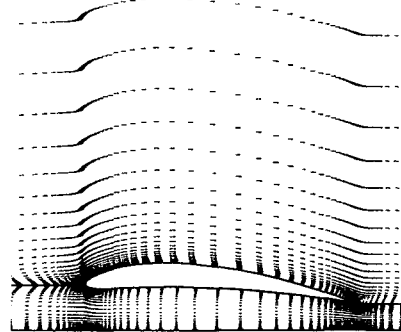


Fig. 11 Velocity field around NACA6409,  $h/c=0.1$

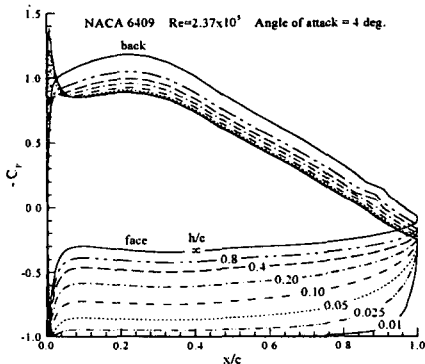


Fig. 9 Pressure distribution on NACA6409

NACA 6409  $Re = 2.37 \times 10^5$  Angle of attack = 4 deg.  $h/c = 0.01$

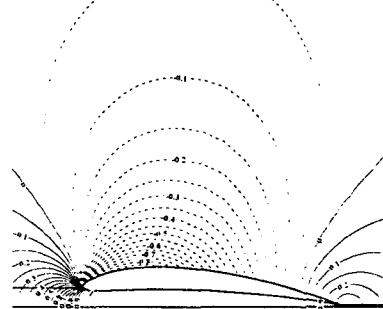


Fig. 12 Pressure field around NACA6409,  $h/c=0.1$



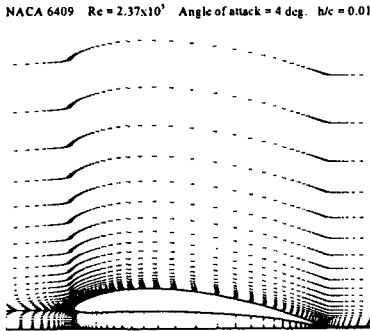


Fig. 13 Velocity field around NACA6409,  $h/c=0.01$

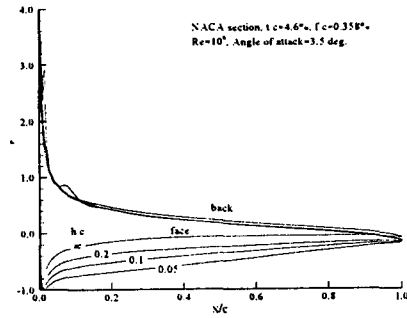


Fig. 16 Surface pressure distributions on the thin wing at different height ratios

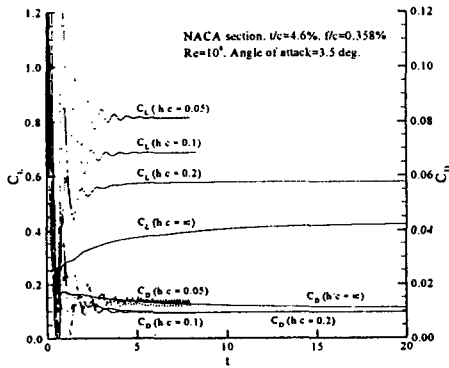


Fig. 14 History of convergence for the thin wing

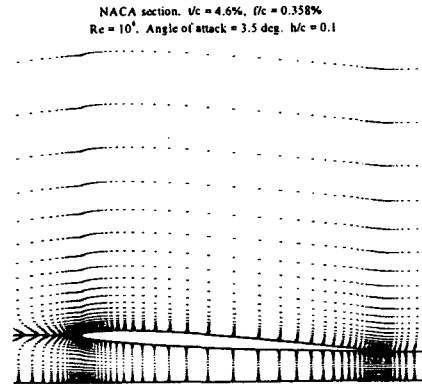


Fig. 17 Calculated velocity field for the thin wing at  $h/c=0.1$

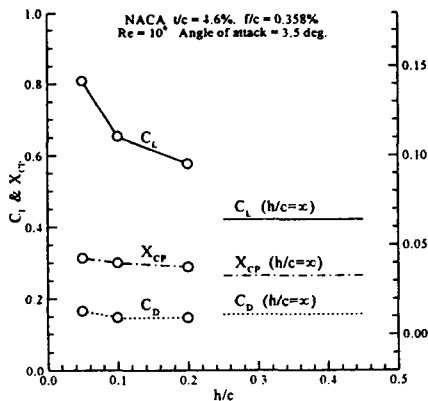


Fig. 15 Variations of lift, drag and pressure center for the thin wing

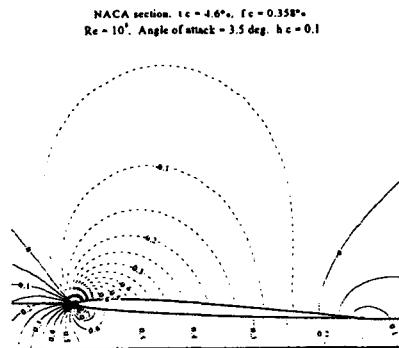


Fig. 18 Calculated pressure field for the thin wing at  $h/c=0.1$